IOP Publishing Measurement Science and Technology
Meas. Sci. Technol. **31** (2020) 045301 (12pp) https://doi.org/10.1088/1361-6501/ab4dee

Development of a fluorescence imaging method to measure void fractions of gas–liquid two-phase flows in a small tube-window for transparent fluids

Liping Huang[1], Shizhe Wen[2], Yanfen Liu[2], Zexi Lin[2] and Zhenhui He[2,3,4]

[1] School of Physics, Sun Yat-Sen University, Guangzhou, People's Republic of China
[2] School of Physics and Astronomy, Sun Yat-Sen University, Zhuhai, People's Republic of China
[3] State Key Laboratory of Optoelectronic Materials and Technologies, Sun Yat-Sen University, Guangzhou, People's Republic of China

E-mail: stshzh@mail.sysu.edu.cn

Received 16 February 2019, revised 6 October 2019
Accepted for publication 15 October 2019
Published 8 January 2020

Abstract

Void fraction is one of the most important parameters to characterize gas–liquid two-phase flow. Yet it has been puzzling people for a long time how to measure it effectively and accurately. In this paper, we develop a fluorescence imaging method that combines the techniques of fluorescence imaging with image processing to measure the two-phase flow cross-sectional void fraction in a horizontal tube window. At first, a tube window is designed and constructed. By illuminating the fluid containing fluorescent dyes inside the tube window with a sheet laser, fluorescence is produced and emits only from the illuminated liquid phase to create a fluorescent light source in the tube cross section. Then, the sequential cross-sectional images of the fluorescent light sources are recorded with a high speed camera equipped with a narrow band filter. Further, the captured images are processed to identify the gas–liquid interface, and to extract the liquid area from the image by segmentation. The cross-sectional void fraction can thus be obtained by comparing the gas area to the total cross-sectional area. Finally, the bulk void fraction can then be indirectly measured by averaging all the cross-sectional void fraction in a given time. Both simulation and experiment were performed to verify and evaluate this method. The simulated cross-sectional images were in good agreement in shape with those observed correspondingly for various flow patterns including slug flow, bubble flow, annular flow and stratified flow. The measured bulk void fractions were in good agreement with those predicted by the slip ratio model and the $k\alpha_{\mathrm{H}}$ model within the range of error, 22% and 14%, respectively, even without a careful calibration of image deformation.

Keywords: visualization measurement, flow pattern, void fraction, fluorescence image, image processing

(Some figures may appear in colour only in the online journal)

[4] Author to whom any correspondence should be addressed.

List of symbols

Nomenclature

A	Image area (mm^2)
C_0	Distribution parameter in the drift-flux model
g	Gravity acceleration
h	Liquid height of a stratified flow (mm)
k	A flow parameter
$\dot{m}$	Mass flow rate ($g\ s^{-1}$)
N	Total number of images
x	Vapor quality
t	Liquid film thickness (mm)
U	Flow velocity ($m\ s^{-1}$)
U_{gm}	Drift flow velocity ($m\ s^{-1}$)

Greek symbols

ϕ_{in}	Diameter of the tube window (mm)
α	Void fraction
α_g	Void fraction in the $k\alpha_H$ model
α_H	Void fraction in the homogenous model
δ	Relative error
ε	Absolute error
ρ	Density ($kg\ m^{-3}$)
σ	Surface tension ($N\ m^{-1}$)

subscripts

b	Bubble
exp	Experiment
fl	Full liquid
g	Gas
i	The ith cross-sectional image
it	Inner tube
l	Liquid
m	Mixture flow
pre	Prediction
sim	Simulation
fls	Fluorescent light source

1. Introduction

Out of many basic parameters in the gas–liquid two-phase flows, void fraction is one of those to provide essential understanding of the flow resistance and the heat transfer characteristics [1]. Yet its accurate measurement is only limited to certain fluid with certain methods, which can be classified into two types: immersion method and non-immersion method.

Common immersion measurement methods include conductance probe methods and optical probe methods. The principle of the conductance probe method is to use the difference of electric conductivity between the gas and the liquid to measure the gas content in the cross section of a two-phase flow [2]. While that of the optical probe method is to use the difference of the refractive indices between the gas and the liquid to judge the phase status at the positions of the probes [3].

However, conductance probe methods only apply to conductive fluids, and the probes could disturb the flow field to some extent for both methods, and lead to imperfect identification of the interface between gas and liquid phases, especially for small tubes. They are thus not suitable for measuring the void fraction in small tubes. Non-immersion measurement methods, such as the radiation attenuation technique, the capacitance method, and the visualization method, are preferred.

The radiation attenuation technique makes use of the radiation attenuation coefficients depending on the phase density. It can be applied to non-transparent tubes or containers. For example, x-ray, γ-ray and neutron [4–6] were attenuated by the fluid inside the tubes to an extent depending on the liquid thickness, making them suitable for measuring void fraction in metallic tubes. Because the equipment is heavy in weight, high in price, and strict in safety and protection, its application has been limited only to special situations.

Capacitance method [7] utilizes the strong difference of dielectric constant between gas and liquid to measure the void fraction. It has the advantage of small in size and light in weight. However, it cannot provide the information of the gas–liquid interface, and has low sensitivity for weak dielectric working medium.

In the experiments of heat transfer of in tube two-phase flows, the flow pattern identified by the gas–liquid interface is a key to understand the high flux heat transfer. One requires to capture movement of the interface of the two-phase flow pattern [8]. Visualization measurement together with image processing technology is capable of capturing the gas–liquid interface of a two-phase flow, independent of the conductivity or the dielectric constant of the fluid.

Ursenbacher *et al* [9–11] developed a non-intrusive method of optical observation and computerized image analysis for the accurate measurement of dynamic void fractions. Experiments were carried out in tubes with the inner diameter of 13.6 mm and 8 mm respectively. In the direction of a vision angle with respect to the flow direction, a digital camera was mount to record the cross-sectional images of the flourescent fluid that was illuminated by a sheet laser. The void fraction data were accurate after image calibration. This method was suitable for stratified flow in a horizontal tube [9] and it was more difficult to apply to smaller tubes, because the liquid film on the upper periphery of the tubular viewing glass causes additional refraction, making calibration difficult.

Inspired by Ursenbacher's effort mentioned above, we attempted to further develop this technique to obtain the cross-sectional void fractions, the bulk void fractions, and the interface between gas and liquid without disturbing the flow field. A small tube window had been designed to observe fluorescence patterns and to measure the cross-sectional void fractions of two-phase flows with further image processing. In this paper, we reported the preliminary results of the void fractions obtained by simulations and experiments in the designed tube window, without image calibration. These sequential cross-sectional images could be used to reconstruct the three-dimensional flow field and to obtain the gas–liquid interface.

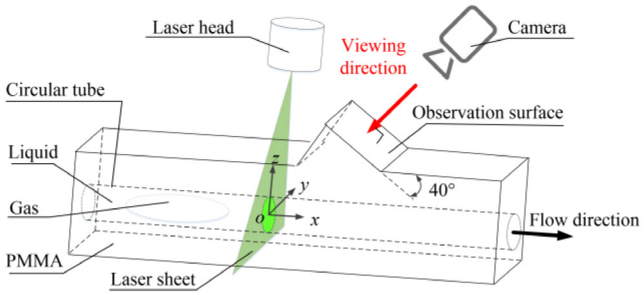

Figure 1. Schematic diagram of fluid imaging of the tube window, the viewing direction is perpendicular to the observation.

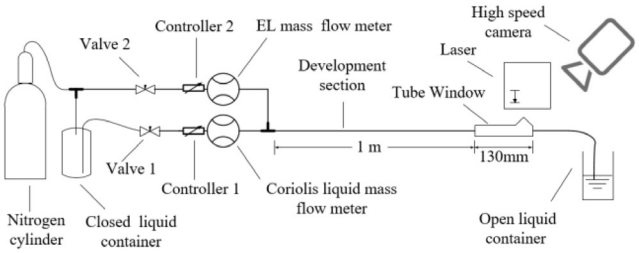

Figure 2. Schematic diagram of the two-phase flow experiment setup: valve 1 and valve 2 is for the rough control of the flow rate of water and gas respectively, while controller 1 and controller 2 for the precise control.

2. Experimental

2.1. Method of fluorescence image

To conduct the required cross-sectional imaging, we designed a tube window (130 mm long, casted and polished by Jiangsu Chenxuan optoelectrics Technology Co., Ltd) with a circular inner diameter (ϕ_{in}) of 4.0 mm and flat external surfaces (figure 1). A rectangular coordinate system is set up in figure 1, with the origin at the intersection point of the fluorescent light source in plane and the tube axis (x) in the flow direction. The gravitional acceleration is along the negative y direction only for the stratified flow, and along the negative z direction for all the other flow patterns. The window has an observation surface, perpendicular to which is the viewing direction, or the direction of observation (shown by the red arrow). The optical axis of the camera is in the viewing direction, and has an angle of 50° with respect to the tube axis.

The presence of fluorescent dyes only exists in the liquid phase is helpful to obtain a clear edge of liquid distribution on the cross section. When excited by the sheet laser, fluorescent dyes in liquid phase will emit the flourescence (regarded below as a fluorescent light source in plane), which passes the tube window (figure 1) and finally reaches the camera to form an image of the fluids cross section.

The cross-sectional void fraction α is defined as the ratio of area occupied by gas (A_g) to the cross-sectional area of the inner tube (A_{it}):

$$\alpha = \frac{A_g}{A_{it}} = 1 - \frac{A_l}{A_{it}} \quad (1)$$

where A_l represents the cross-sectional area occupied by liquid phase, or $A_{it} = A_g + A_l$.

2.2. Modelling

ZEMAX is a powerful general-purpose optical system design tool with a non-sequential component that can be used for imaging analysis for complex CAD models. It was used to simulate the camera image for the tube window design. The subjects of ZEMAX simulation mainly include: the tube window, the fluorescent light source (the fluorescent cross section of the transparent fluid, representing the fluorescent dyes excited by the sheet laser.), and the detector (the camera).

The 3D tube window model (figure 1) was imported into ZEMAX (Zemax OptisStudio 18.7) as the object (a nuon defined by the ZEMAX), which was the medium that affected the propagation of light. The light propagates according to the actual characteristics that intersected with the tube window. The size and the material (polymethyl methacrylate) is the same as those of the manufactured tube window. The major image schematic of the simulation is also the same as the experimental set-up shown in figure 3.

The fluorescent plane that represents the liquid cross section will changes with time when a two-phase flow passes through the window. In ZEMAX, we used a fluorescent light source in plane to represent the liquid cross section illuminated by the sheet laser. The thickness of the fluorescent light source was set as 0.01 mm, other than the laser light thickness of 0.25 mm used in the experiment. The setting of the fluorescent light source thickness in simulation was based on the consideration of the simulation precision that depends on the number of the layout rays in the model. The number of the layout rays becomes less with the increase of the thickness of the fluorescent light source. Take the simulation of the slug flow for example, if the thickness is set as 0.25 mm, the relative error of the cross-sectional void fraction was 35% with respect to that of the slug head fluorescent light source. This error was much larger than (2%), the relative error of the same slug head light source with the thickness of 0.01 mm.

The effect of the tube-window on the fluorescent light was obtained through the ray tracing function of ZEMAX. When a beam of light reaches the detector, the ray positions are recorded; the spatial position and the intensity of the light are thus obtained.

2.3. Experimental setup

As shown in the schematic diagram of the setup in figure 2, the nitrogen-water two-phase fluid is created by mixing the outflowing nitrogen from the nitrogen bottle with the water driven by the compressed nigtrogen. The mixed fluid is developed to a stationary and stable two-phase flow with certain flow patterns by passing through a horizontal stainless tube (with the inner tube diameter of 4.0 mm and the length of 1.0 m). The steady two-phase fluid then flows through the tube window for observation, and is finally collected by an open container for the separation of the liquid from the gas by gravity. The separated water would be injected into the closed liquid container for recycling. The separated nitrogen is directly discharged into the atmosphere.

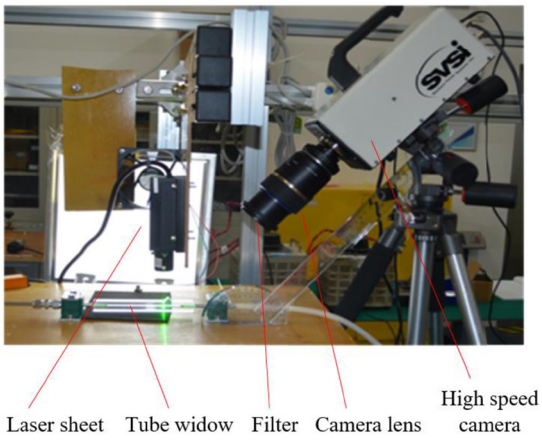

Figure 3. The experimental set-up for recording the dynamic cross-sectional fluorescence images of the nitrogen-water two phase flows.

When fluorescent dyes is dissolved in the water and excitated by the sheet laser, it emits flourescence. The flourescence is allowed to pass the transparent water, then the tube-window, the filter on the camera lens, which filters out the laser and the environment light, and the lens. It finally forms an image of the fluids cross section on the camera (see figure 2).

An experimental setup was built to establish the controlled gas–liquid two-phase flow and to record the corresponding fluid cross-sectional images (figures 2 and 3), with the same schematic shown in figure 1. The intersection point of the fluorescent light source and the tube axis was the origin coordinate of the coordinate system, the sheet laser was perpendicular to the tube axis, and the Laser head is about 50 mm away from the origion cordinate. Rhodamine 6G (QuZhou Rainfull Chemical Co., Ltd; Specifications: British Standard) was dissolved in deioned water in the concentration of 10^{-6} mol l^{-1} as fluorescent dyes in the experiment.

In the experiment, the sheet laser in used was MGL-532-III (Changchun New Industries Optoelectronics Technology Co., Ltd; with output power of 301.4 milliwatt, TTL modulation option). It is a continuous line type laser, i.e. when the power supply is switched on, the laser is in continuous working state without any control signal input. The wavelength of the laser beam is 532 nm and the beam diameter is 0.2 mm (from the supplier). A lens (Changchun New industries Optoelectronics Co., Ltd, Linear Prism) with a full angle of 30 degrees was mounted on the output aperture of the laser. When the laser beam passed through the lens, it was spread to a line form, i.e. a sheet laser, with the measured thickness of 0.25 mm by projecting the sheet laser on a white paper. A monochrome high speed camera was used: the SVSI GIGAVIEW (Southern Vision Systems, Inc., with the readout model of ROI), with a CMOS sensor of a bit depth of 10 and a TAMRON SP AF 90 mm camera lens. The camera was set to operate at an aperture of 2.8, with an image resolution of 128 × 128 at the sample rate of 500 frames s^{-1}. The distance between the camera lens and the origin coordinate was about 300 mm (the focal length range was 90 mm, the nearest focus distance was 290 mm). A narrow band filter with the cutoff wavelength of 532 nm (BP554, Shenzhen Saixu Photoelectric technology Co.) was mount in front of the camera lens, to filter out the reflected laser light and the environment light on the fluorescence imaging.

The flow patterns depend on the pressure, the flowrate of the liquid and that of the gas respectively. In the experiment, the pressure was close to one atmosphere, depending on the flowrate and the flow pattern of the fluid, but not higher than 106 kPa. The flowrate of water was measured and controlled online with a Coriolis flowmeter and a controller (MINICORI-FLOW MFC, M14-RGD-33K-S+C5I-ITU); while that of the nitrogen with another Coriolis flowmeter and controller (EL-FLOW F-201AV-50K-RAD-33-V), respectively. The flow range of the flowmeter (with a controller) in the water path was 0.4–20 Kg h^{-1} with an accuracy of ±0.2% Rd (0.01 g s^{-1} for water); while that in the nitrogen path was 0–50 l min^{-1} with an accuracy of ±0.5% Rd plus ±0.1% FS (0.001 g s^{-1} for nitrogen). The two flowmeters can also measure the density of the fluid which pass through with an accuracy of 0.001 kg m^{-3}. All the flowmeters and controllers were linked to a PC for flowrate data acquisition (unit in g s^{-1}). The gas flow rate was adjusted from 0.002 g s^{-1} to 0.010 g s^{-1} at room temperature; while the liquid flow rate range from 2.13 g s^{-1} to 3.33 g s^{-1}. Two-phase flow patterns, such as slug flows, bubble flows, annular flows, and stratified flows, were respectively obtained by adjusting the flowrate of the water and that of the nitrogen respectively.

For a full-liquid image, the number of pixels of the liquid part was 1091, which occupied only 6.7% of the total number of the full image pixels. After image processing, the cross-sectional void fractions were obtained based on the definition of equation (1). The bulk void fraction was obtained by averaging the sequential values of the cross-sectional void fractions:

$$\alpha_{\mathrm{exp}} = \frac{\sum_1^N \alpha_{\mathrm{i}}}{N} \tag{2}$$

where N is the number of the selected sequential cross section, α_{i} is the cross-sectional void fraction of the ith cross section.

The obtained bulk void fraction α_{exp} was taken as the measured value without image deformation calibration. One can thus define the relative error (δ_{exp}) between the measured value and the predicted value:

$$\delta_{\mathrm{exp}} = \frac{\alpha_{\mathrm{exp}} - \alpha_{\mathrm{pre}}}{\alpha_{\mathrm{pre}}} \tag{3}$$

where α_{pre} is the model-based predicted void fraction.

2.4. Image processing

In this experiment, the image processing toolkit in MATLAB (R2018b) was used for image processing includes threshold segmentation and feature extraction [12, 13].

Threshold segmentation converts an original recorded image (gray in color) to a binary image that shows black and white only, representing the gas phase and the liquid phase respectively. The boundaries of the black and white regions in a binary image depend on the selected threshold of gray level in the gray histogram of the image.

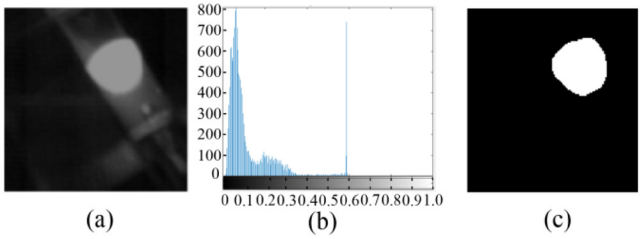

Figure 4. Cross-sectional images: (a) the gray image for the full liquid; (b) the gray histogram, where the ordinate represents the number of pixels, and the abscissa represents the gray level of pixels (0–1.0); (c) the binary image.

In the experiment, the cross-sectional flourescent image must be the brightest in the photo, because the fluorescence (the third peak with the gray level of 0.60 in figure 4) comes from the fluorescent dyes excitated by the sheet laser. Although the environment light (the first peak with the gray level of 0.05 in figure 4) that was not completely filtered out and the planar reflected fluorescence from the surfaces of the transparent tube window (the second peak with the gray level of 0.20 in figure 4) can pass the filter, their gray level was obviously lower. In other words, at least three peaks of the pixel appeared in the gray histogram at different gray levels for the cross-sectional images of full liquid flow. Such distribution character of the gray histogram can be used to define a threshold for the segmentation: first, the threshold must be in the valley between the peak at the highest gray level (representing the fluorescence) and that at the next peak; second, the void fraction should be the most insensitive to the selection of the threshold in the valley. For the cross-sectional images of the full liquid flow shown in figure 4, the appropriate threshold should be in the valley ranging from 0.25 to 0.60. The sensitivity analysis showed that the uncertainty of the void fraction (or the pixel number) was the smallest near the threshold of 0.45 (within $\pm 6.0\%$ when the threshold section varies ± 0.05). As a result, for the captured full-liquid fluorescence image, 0.45 was selected as the threshold segmentation to produce the binary image (figure 4(c)). For a slug flow, the curve surface of the slug bubble tail could reflect and focus fluorescence light, to produce high intensity spots somewhere. Such spots cannot be omitted by threshold segmentation easily because they are from the focused fluorescence. Therefore, feature extraction was introduced to solve the problem.

More complicated than in the simulation, the pure spectrum of the laser, the uniformity of the laser cross-section distribution in the tube, the smoothness of the window surface, and the purity of the fluorescent indicator may all affect the imaging quality to a certain extent in the experiment. As a result, there might not be an universal fixed threshold. Personal judges had to be involved in the threshold segmentation, which not only increased the workload, but also inevitably introduced subjective errors. The tube window should be improved, e.g. by a black coating on the surface to reduce the reflected fluorescence; or machine learning could be a good choice to resolve the problems, especially in batch processing. However, they are the other research issues in the future.

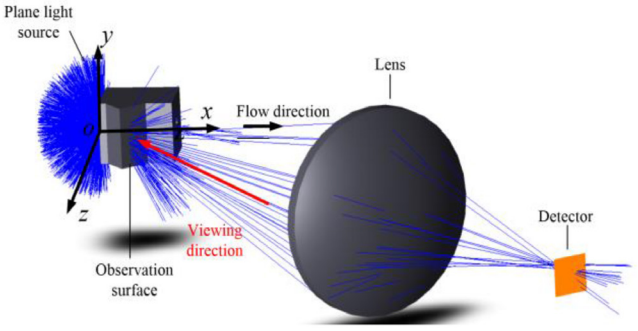

Figure 5. Model configuration of the tube window and detector for simulation, the viewing direction is perpendicular to the observation, the gravitional acceleration is along the negative y direction only for the stratified flow, and along the negative z direction for all the other flow patterns.

For simulation, because the wavelength of light was unique and there was no interference from outer stray light, we should choose a fixed threshold based on the same method. The liquid boundary line in the middle of a slug flow is relatively long as compared to the liquid area, a slug flow is a good candidate for sensitivity analysis of threshold segmentation. The result showed that the change of the cross-sectional void fraction caused by the change of threshold was the smallest near the threshold of 0.40 (within $\pm 6.5\%$ when the threshold section varies ± 0.05). So 0.40 was selected as the threshold for threshold segmentation for all the simulated images.

Feature extraction can effectively separate the target features from the useless information (noise) by identifying and deleting the alien features as noises (e.g. circularity and the number of pixels). It can exclude those bright noises that can not be cut out by threshold segmentation, because such noises are indirectly from the fluorescence, especially due to the reflection of the fluorescence by the curved gas–liquid interfaces like the slug tail interface. There were four kinds of feature of the bright noises: ellipses, dots (or spots), strips, and bars. The noise region with small area such as a dot or a spot was omitted by the feature of pixels number. Except for cases of the annular flow and the slug middle, any strip or bar with circularity far smaller than 1 was omitted by circularity criterion.

The preserved bright target represented the cross section of the liquid, and the cross-sectional void fraction was obtained by counting the number of its pixels and deviding it by the total with equation (1).

3. Results and discussions

3.1. Simulation

Shown in figure 5, the structure of window imaging for simulation consists of a fluorescent light source to simulate the dye flurescence, a tube window that is the same as that used in the experiment, a lens and a detector to simulate the camera lens that focuses layout rays onto the camera detector. The rectangular coordinate system is the same as that shown in figure 1, with the origin at the intersection point of the fluorescent

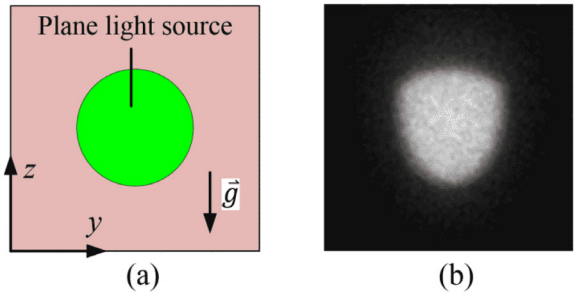

Figure 6. The fluorescent light source (a) and the simulated cross-sectional image (b) for the full liquid flow.

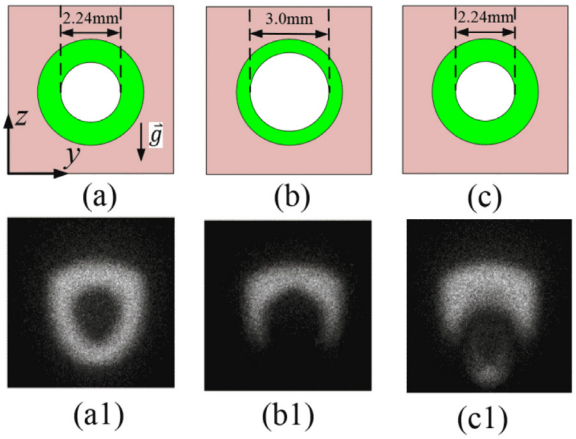

Figure 7. The fluorescent light sources ((a)–(c)) and the simulated cross-sectional images ((a1)–(c1)) of the slug flows: (a) and (a1) for the slug head; (b) and (b1) for the slug middle; (c) and (c1) for the slug tail.

light source and the tube axis (x) in the flow direction. The optical axis of the lens and the detector is perpendicular to the observation surface of the window. The common flow patterns were selected for simulation: the full liquid flow, the slug flow, the bubble flow, the annular flow, and the stratified flow. The selected simulated images presented below are representative.

To simulate the full liquid in the model, a liquid cylinder with the diameter of 4.0 mm was inserted into the tube. The corresponding fluorescent light source and the simulated image are shown in figures 6(a) and (b) respectively. The image composed of white pixels are formed by the light that emits from the fluorescent light source (the green parts in the Figures) and reaches the detector. Because the light is refracted at the curve interface between the liquid phase and the window tube, the image in figure 6(b) is distorted from the circlar fluorescent light source and looks like a shield.

When the slug flows along the positive x direction, the head, the middle, and the tail of the slug reaches the light plane in sequence, leading to the fluorescent light source varies correspondingly as the liquid part of the slug flow passes through. An ellipsoid with a semi long axis (a, along the x axis, the tube axis) and a semi short axis (b, parallel to the y-O-z plane) is used to describe a slug or a big bubble. It can be expressed in a mathmatical equation:

$$\frac{(x-vt)^2}{a^2}+\frac{y^2+z^2}{b^2}=1 \tag{4}$$

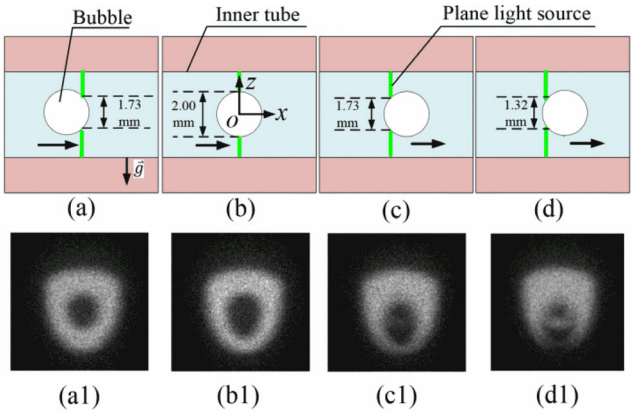

Figure 8. The fluorescent light sources ((a)–(d)) and the simulated cross-sectional images ((a1)–(d1)) for the bubble flow: (a) and (a1) for the head of the big bubble; (b) and (b1) for the middle of the big bubble;(c) and (c1) for the tail of the big bubble.

where v is the mean speed of the bubble.

The slug for simulation was set as $a = 3.0$ mm and $b = 1.5$ mm. Three representative fluorescent light sources were selected to simulate the liquid cross sections for the head, the middle, and the tail of the slug flow, respectively (figures 7(a)–(c) in green). The sizes of the cross sections of the slug are given in figures 7(a)–(c). The cross-sectional image of the slug head looks like a shield with a big hole (without white pixels) in the middle of the image (figure 7(a1)). This agrees with the fluorescent light source of the slug head after considering the deformation of the image. The cross-sectional images of the slug middle and the slug tail are incomplete (figures 7(b1) and (c1)), leaving an opening region at the bottom of the deformed ring pattern, and a bright ellipse appears in the blank region of figure 7(c1). The light from the upper part of the source can form its image on the detector, but that from the bottom part cannot. When the gas part of the slug flow moves into the light path to the detector, the curve gas liquid interface deflects the light from the bottom, making it impossible to reach the detector. So the bright ellipse at the bottom part of figure 7(c1) is caused by the reflection and refraction of the fluorescence by the slug bubble's curve interface, which should be omitted after threshold segmentation and feature extraction.

To simulate bubble flows in the model, gas bubbles were inserted into the liquid cylinder in the full liquid model. Only the simply cases of single bubble and two bubbles were considered. In the case of single bubble, the diameter of the gas bubble was 2.0 mm, at four positions with respect to the light plane (figures 8(a)–(d)), respectively. In the case of two bubbles, the diameters of the bubbles were both 1.0 mm; one of them located at the center of the light plane, the other at four different positions with respect to the first (figures 9(a)–(d)), respectively.

Figures 8(a1)–(d1)) shows the corresponding simulated cross- sectional images of the single bubble with the diameter of 2.0 mm, each looks like a shield with a hole inside. The hole represents the cross section of the gas bubble. In figure 8(d1), an opening region appears at the bottom of the shield, and a bright strip appears in the inner hole of the shield. They were

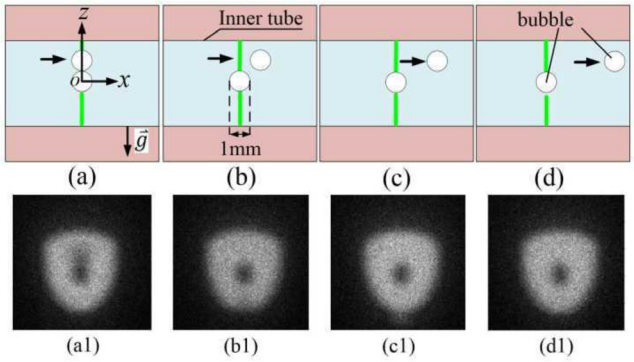

Figure 9. The fluorescent light sources ((a)–(d)) and the simulated cross-sectional images ((a1)–(d1)) for the bubble flow with one bubble in the center (0,0,0) and another located at (0,0,1.5) for (a) and (a1), (1,0,1.5) for (b) and (b1), (2,0,1.5) for (c) and (c1), (4,0,1.5) for (d) and (d1), respectively.

caused by the reflection and refraction of the tail curve interface of the bubble.

By taking into account the deflection of light by the other bubble at the positions shown in figures 9(a)–(d) with coordinates, the cross-sectional images of the fluorescent light sources are obtained for the two-bubble case (figures 9(a1)–(d1)). With the shift of the upper bubble position, the image displays slight deficiency, and then slight surplus at the bottom of the fluorescence image.

To simulate the annular flows with different thickness (t) of liquid film, gas cylinders with different diameters were inserted into the liquid cylinder in the model. Two liquid films thickness of 0.2 mm and 0.1 mm were set by respectively inserting a gas cylinder of 3.6 mm and 3.8 mm in diameter into the liquid cylinder coaxially. The corresponding fluorescent light sources are established (the green rings in figures 10(a) and (b)). The cross-sectional images of the annular flow are incomplete (figures 10(a1) and (b1)), leaving an opening region at the bottom of the deformed ring image, for the same reason as discussed in the slug flow. In fact, the simulation for the annular flow can be applied to that of the middle of a long slug.

For stratified flow, to reduce any gas–liquid interface that refract light to the camera, the tube window setup, together with high speed camera and the coordinate system, was rotated by 90°, i.e. to observe the flow pattern in horizontal direction. The light path from the fluorescent plane to the camera was then in palleral to gas–liquid interface of the stratified flow to eliminate light refraction. The shape of the fluorescent light source of the stratified flow depends on the liquid height (h). Two representative fluorescent light sources were established to simulate the fluorescence cross sections with the liquid height of 0.25 d_{it} and 0.50 d_{it}, respectively (the semicircle parts in green figures 11(a) and (b)). The simulated cross-sectional images agree with the fluorescent light sources in shape with the height of 0.25 d_{it} and 0.50 d_{it}, by taking into account the image deformation (figures 11(a1) and (b1)). For comparison, the simulated cross-sectional image of full liquid

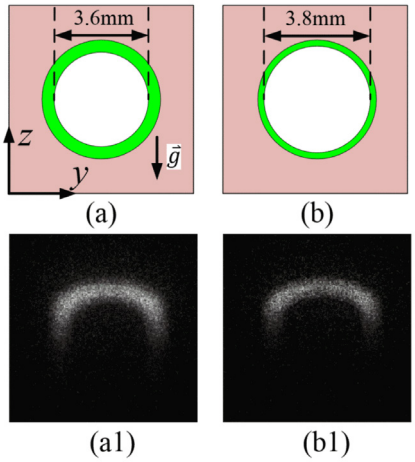

Figure 10. The fluorescent light sources ((a) and (b)) and the simulated cross-sectionall images ((a1) and (b1)) for the annular flow.

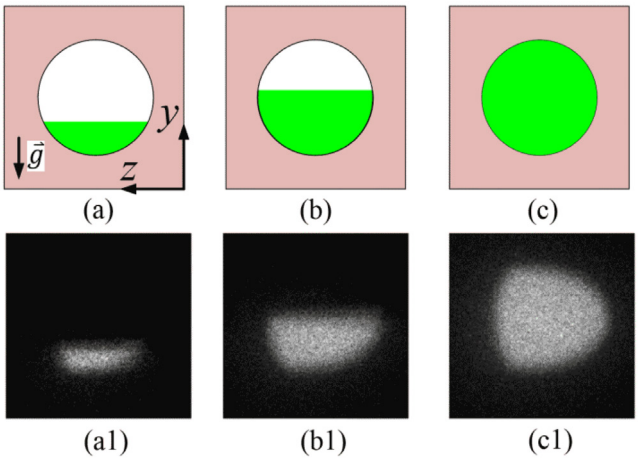

Figure 11. The fluorescent light sources ((a) to (c)) and the simulated cross-sectional images ((a1)–(c1)) for the stratified flow: $h = 0.25\ \phi_{in}$ for (a) and (a1); $h = 0.50\ \phi_{in}$ for (b) and (b1); full liquid (c) and (c1) for comparison.

flow (figure 11(c1)) also agrees in shape with the fluorescent light source in this model (figure 11(c)).

We define δ_{sim} as the relative error of α_{sim} with respect to α_{fls}, ε the absolute error of α_{sim} to α_{fls}:

$$\delta_{sim} = \frac{\alpha_{sim} - \alpha_{fls}}{\alpha_{fls}} \tag{7}$$

$$\varepsilon = \alpha_{sim} - \alpha_{fls}. \tag{8}$$

Table 1 lists the source void fractions (α_{fls}) and simulated cross-sectional void fractions (α_{sim}) for all kinds of flow patterns, with the gray level threshold of 0.40 for simulated image segmentation.

For the fluorescent light sources of the annular, the slug middle, the slug tail, and the tail of the bubble with a diameter of 2.0 mm (or larger), all the simulated images left an opening region at the image bottom. This was mainly related to the large gas region located in the path of light from the

Table 1. The relationship between the simulated cross-sectional void fractions with the threshold of 0.40 and the fluorescent light sources void fractions for the selected samples.

Flow pattern	Size (mm)	Center of bubble	α_{pls}	α_{sim}	ε	δ_{sim} (%)
Slug flow	Half long axis 3.0	Head (−2,0,0)	0.31	0.30	−0.01	−3.2
	Half short axis 1.5	Middle (0,0,0)	0.56	0.69	0.13	22
		Tail (2,0,0)	0.31	0.50	0.19	60
Bubble flow		Head (−0.5,0,0)	0.19	0.18	−0.01	−5.2
	d_b =2.0	Middle (0,0,0)	0.25	0.24	−0.01	−4.0
		Tail (0.5,0,0)	0.19	0.32	0.14	75
		Tail (0.75,0,0) upper bubble	0.11	0.20	0.09	82
Two bubbles	d_b =1.0	(1,0,1.5)	0.06	0.13	0.06	1.0×10^2
		(2,0,1.5)	0.06	0.03	−0.04	−57
		(4,0,1.5)	0.06	0.05	−0.02	−28
Annular flow	$t = 0.2$ mm	—	0.90	0.93	0.03	3.1
	$t = 0.1$ mm	—	0.81	0.83	0.02	2.9
Stratified flow	$h = 0.25\ d_{it}$	—	0.80	0.88	0.08	9.5
	$h = 0.50\ d_{it}$	—	0.50	0.51	0.01	2.0

Table 2. Bulk void fraction of five fragments.

Flow patterns		Bulk void fraction from image processing				
Slug flow	α_{exp}	0.69	0.70	0.65	0.62	0.68
Water: 3.33 g s^{-1}	Number of images	42	48	42	58	64
N_2: 0.010 g s^{-1}						
Bubble flow	α_{exp}	0.39	0.34	0.37	0.36	0.37
Water: 2.37 g s^{-1}	Number of images	77	68	40	63	50
N_2: 0.002 g s^{-1}						
Annular flow	α_{exp}	0.76	0.78	0.68	0.70	0.72
Water: 2.13 g s^{-1}	Number of images	68	64	65	78	80
N_2: 0.010 g s^{-1}						

fluorescent light source to the camera for any of those patterns: the curve gas–liquid interface of the pattern deflected the light from the source's bottom, leading to a deficiency of the liquid in the image, and thus a significant and positive relative error of the void fraction.

Particularly, when the light source located in the middle or the tail of a slug, or the tail of a big bubble, the light deflection led to the biggest absolute errors of the void fraction. Although the errors of void fraction for a slug tail and a big bubble tail were large, their contribution to the bulk void fraction was small, because the time a tail took to pass the illuminated section was short as compared with that for the whole slug. For the slug flows with parameters shown in table 1, if the time proportion of head, middle and tail is 3:6:1, the bulk void fraction is 0.46 and 0.55 for the fluorescent light source and the simulated image, respectively. The relative error is 20%, a neglectable deviation for many applications. If the time proportion is 1:1:1, the bulk void fraction becomes 0.39 and 0.66, respectively for the fluorescent light source and the simulated image. This produces an unneglectable relative error of 69%.

In the cases of two small bubbles with the diameter of 1.0 mm (figure 9), the simulated images left an expanded region near the hole related to the bubble located at the center of the illuminated cross section. This might due to the deflection of light by the other bubble located in the light path to the camera. The resulting error of void fraction can be positive or negative, depending on the position of the other bubble. Despite the relative error of the local cross-sectional void fraction was large in some case (even up to 100%), the void fraction itself and its absolute error was relatively small.

For the stratified flow, the relative error was less than 10%. Because of the limited number of layout rays from randomly generated source, the analysis rays were rare in the simulation, and the fluctuation was large in the image. The edge of the binary image obtained by threshold segmentation was not smooth. It is one of the contributions to the simulation errors.

The simulated results support the idea that the designed window is capable of observing cross-sectional images of various flow patterns, such as slug flow, bubble flow, annular flow, and stratified flow. Although there are deformation and deficiency in the simulated images, the obtained cross-sectional void fraction shows that it could be acceptable for the bulk void fraction in an error range smaller than those of the cross-sectional void fractions because of the average effect.

As a result, we consider to simplify the calculation of the bulk void fraction by ignoring the calibration of image deformation. We will investigate the effectiveness of such simplification by experiment in the following section.

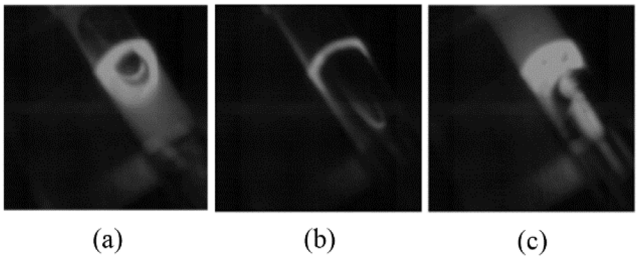

Figure 12. The cross-sectional camera images of a slug head (a); a slug middle (b); and a slug tail (c).

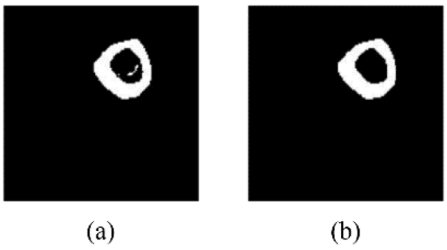

Figure 13. The image processing for the slug head: after threshold segmentation (a); after the feature extraction (b).

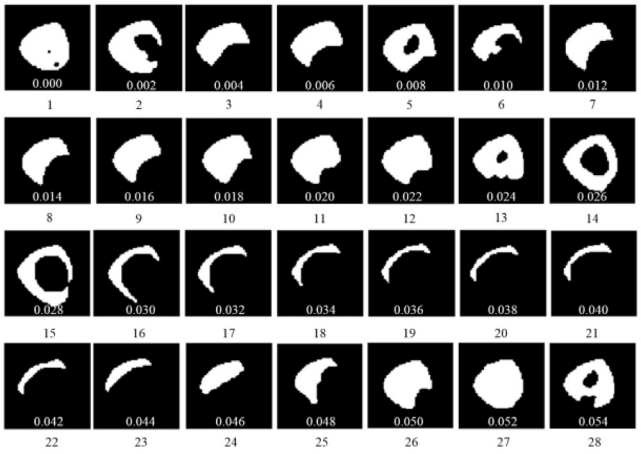

Figure 14. The 28 consecutive cross-sectional images of a bubble flow in the recorded time from 0.000 s to 0.022 s, and a slug flow from 0.024 s to 0.052 s after threshold segmentation.

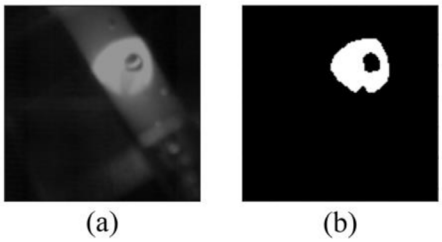

Figure 15. The image of the bubble flow before processing (a), the gray image; and after processing (b), the binary image.

3.2. Measurement of the bulk void fractions

By mixing the water containing fluorescent dyes with nitrogen gas, a slug flow was formed, which produced a series of representative cross-sectional images (table 2) at the tube window illuminated by the sheet laser, including the slug head in figure 12(a), the slug middle in figure 12(b), and the slug tail in figure 12(c).

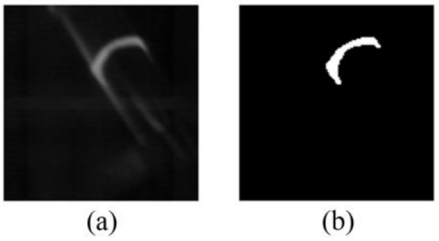

Figure 16. The cross-sectional images of the annular flow before processing (a), the gray image; and after processing (b), the binary image.

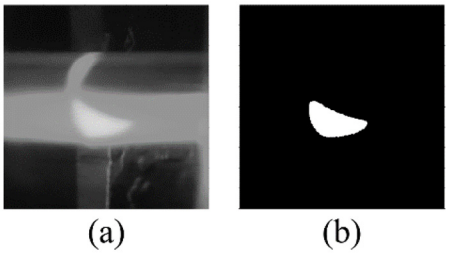

Figure 17. The cross-sectional image of the static stratified flow before processing (a), the gray image; and after processing (b), the binary image.

This bright shield pattern in figure 12(a) is the target which must be preserved during image processing. The surroundings with low brightness were from the stray light caused by the diffuse reflection of the tube window and were omitted after threshold segmentation as shown in figure 13(a), where there is a hole in the middle of the bright shield and a bright strip appears in the hole. The strip should be caused by the refraction on the slug's curve interface, and were omitted after the feature extraction (figure 13(b)).

After image processing, consecutive cross-sectional images were obtained. Shown in figure 14 is one of the examples. The 28 consecutive images could be used to reconstruct the flow pattern and calculate the bulk void fraction. From the image character, one can identify a bubble flow (from 0 to 22 ms) transforming to a slug flow (from 24 to 52 ms).

For the slug flow, 254 cross-sectional images in five periods (consecutive in every periods) were intercepted for image processing (table 2). The average cross-sectional void fraction (based on equation (2)) was 0.67 with standard deviation of 0.04.

Figure 15 shows the cross-sectional images of bubble flow (table 2) formed by mixing water with nitrogen. The bright 'shield' in figure 15(a) is one of the cross-sectional images of the bubble flow. The bubble refracted the sheet laser, and resulted in the non-uniformity of light intensity below the bubble, leading to an deficient region at the image bottom, especially for large bubble. The blank spot in the bright shield represents the cross section of the bubble. The bright strip in the hole (figure 15(a)) was caused by the reflection and refraction on the bubble' curve surface and was omitted by the feature extraction (figure 15(b)).

Table 3. Model summary and correlation formula.

Model (author)	Formula	The proportion within the relative error of ±15%	Measurement method
Slip ratio [14]	$\alpha = (1 + \frac{1-x}{x}\frac{\rho_g}{\rho_l}(0.4 + 0.6\sqrt{\frac{\frac{\rho_l}{\rho_g}+0.4\frac{1-x}{x}}{1+0.4\frac{1-x}{x}}}))^{-1}$	96% [15]	Quick closing valves
Homogeneous [16]	$\alpha_H = (1 + \frac{1-x}{x}\frac{\rho_g}{\rho_l})^{-1}$	100% [17]	Computational model
$k\alpha_H$ [5]	$\alpha_g = k\alpha_H$ $k = 0.833 + 0.167x$	89% [15, 18]	Quick closing valves
Drift flux correlations [19]	$\alpha = \frac{U_{sg}}{C_0 U_m + U_{gm}}$ $C_0 = 1 + 0.121 - x$ $U_{gm} = \frac{1.18(1-x)}{\rho_l^{0.5}}(g\sigma(\rho_l - \rho_g))^{0.25}$ $U_m = U_{sg} + U_{sl}$	83% [5, 17, 19–21]	—

Table 4. Comparison between the measured void fractions from image processing ($\alpha_{\_exp}$) and those calculated with model formula.

Flow patterns	Bulk void fraction from image processing		Bulk void fraction from flow models			
			Slip ratio	$k\alpha_H$	Drift flux	Homogeneous
Slug flow	α_{exp}	0.67	0.55	0.59	0.53	0.71
	δ_{exp}		+22%	+14%	+26%	−6%
Bubble flow	α_{exp}	0.37	0.32	0.34	0.23	0.40
	δ_{exp}		+16%	+9%	+61%	−8%
Annular flow	α_{exp}	0.73	0.62	0.66	0.58	0.79
	δ_{exp}		+18%	+11%	+26%	−8%

Similarly, 298 cross-sectional images in five periods (consecutive in every periods) of the bubble flow were intercepted for image processing (table 2). The average cross-sectional void fraction was 0.37 with standard deviation of 0.02.

Figure 16(a) shows one of the sequential cross-sectional images of an annular flow (table 2) formed by mixing water with nitrogen. The image is an incomplete ring, leaving an opening region at the bottom to form a bright U-shape strip. It is the target representing the upper liquid film of the annular flow.

Similarly, 355 cross-sectional images in five consecutive periods of an annular flow were selected for the image processing (table 2). The average cross-sectional void fraction was 0.73 with a standard deviation of 0.05.

Figure 17(a) shows a cross-sectional gray image of a static stratified flow, with the tube window's orintation the same as that in the simulation (gravity along the negative y direction). The brightest semilunar pattern at the bottom represents the liquid of the horizontal stratified flow, and the surroundings in gray is mainly from the liquid out of the illuminated cross section, which was excitated by the reflected and scattered laser. It was omitted after the feature extraction (figure 17(b)). The cross-sectional void fraction of the stratified flow was 0.74.

After the image processing, the obtained fluorescent cross-sectional images of the in-tube two-phase flow agreed quite well in shape with those obtained by simulation for all of the investigated flow patterns.

The sequential images selected to calculate the bulk void fraction for each of the flow patterns were within one period approximately. Because of the imperfect periodical repeat of the flows, the uncertainty of the chosen time period should have reduced the accuracy of the measurement. For higher accuracy, one should use much longer interval to obtain the average void fraction. Computer automatic image processing based on machine learning could be helpful to finish this task much more efficiently in the future.

3.3. Comparison with model predictions

In the experiment, Nitrogen with the mass flow rate of $\dot{m}_g$ was mixed with water with the mass flow rate of $\dot{m}_l$ to develop a two-phase flow (figure 2). The quality (x) is defined as the gas mass flow rate $\dot{m}_g$ over the total mass flow rate ($\dot{m}_g + \dot{m}_l$).

$$x = \frac{\dot{m}_g}{\dot{m}_g + \dot{m}_l} \tag{9}$$

When the quality, the densities, and the viscosities of the gas phase and the liquid phasse are known, we can predict the void fraction based on the models with well-verified correlation formulas.

Four common models were selected for the prediction of the void fraction of the nitrogen-water two-phase flow: the slip ratio model, the $k\alpha_H$ model, the drift flux model, and the homogeneous model (summarized in table 3).

In the slip ratio model [18], the ratio of the actual velocity of gas to that of the liquid is defined as the sliding speed ratio. The void fraction α is a function of vapor quality x defined in equation (9), the gas–liquid density ratio (ρ_g/ρ_l where ρ_g is the gas density and ρ_l the liquid density), and the gas–liquid viscosity. Based on the slip ratio model, Smith [14] proposed

a formula for the calculation of the void fraction suitable for various flow patterns.

In the $k\alpha_H$ model, Massena *et al* defined the void fraction α_g as the parameter proportional to the void fraction of non-slip homogeneous flows α_H with a coefficient k (a fluid parameter) when they studied the gas–liquid two-phase flows [5].

The drift flux model defines the void fraction with the distribution parameter C_0 (non-uniformity of flow), surface tension (σ), drift velocity U_{gm} (the velocity ratio of gas phase to liquid phase, the gas phase superfical velocity $U_{sg} = \frac{\dot{m}_g}{\rho_g A_{it}}$ (the ratio of gas phase volume flow rate to the cross-sectional area of the flow channel), and liquid phase superfical velocity $U_{sl} = \frac{\dot{m}_l}{\rho_l A_{it}}$ (table 3).

Together with those (α_{exp}) obtained from the camera image process, the model-based calculated void fractions (α_{pre}) are listed in table 4 for slug flow, bubble flow, and annular flow, respectively.

Compared with those calculated with the homogeneous model, the bulk void fractions obtained from the camera image process gave the negative and the smallest deviation (less than 10%). Because the deficiency of the liquid image will inevitably lead to the increase in the void fraction, i.e. a significant positive systematic error, such a small and negative deviation may indicate that the homogeneous model is not suitable to predict the bulk void fraction in the experiment.

Compared with the other three models, all the measured void fractions have positive relative errors with respect to the model prediction: within the range of 26%–61% for the drift flux model; 16%–22% for the slip ratio model; and 9%–14% for the $k\alpha_H$ model. Those models have been verified by the method of quick closing valves. This indicates that the measured void fractions based on the simplified image processing method are acceptable.

In the process of laser propagation, due to the reflection and refraction of the curved gas–liquid interface to the laser beam, the intensity of the laser light in the region behind a bubble became weak and not uniform in the illuminated cross section. For the same reason, the fluorescence from the bottom was deflected by the curved bubble's surface. The combination of the two effects led to the deficient bottom part of the fluorescence image. This should be the major contribution of the systematic error of the void fraction measurement for the simplified method. The issue of laser inhomogeneity and imaging integrity would be resolved by extended design of the structure of the tube window in the future. The calibration of the deformed cross-sectional image is our next effort for the potential reduction of the errors.

4. Conclusions

For a transparent two-phase flow through a tube window, only the liquid of which contains homogenous diluted fluorescent dyes, the cross-sectional fluorescence images produced by a sheet laser on the liquid were obtained by simulation using ZEMAX, and by a high speed camera. The images obtained in the experiment agreed quite well in shape with those by simulation. This supported the idea that the designed window allows the observation and the capture of the cross-sectional images for various flow patterns including slug flows, bubble flows, annular flows, and stratified flows. By combining the fluorescence measurement technology with the simplified image processing for the recorded sequential images without the calibration of the deformed image, we made it possible to measure the bulk void fractions with an acceptable precision:

1. The relative error of the simulated cross-sectional void fractions were within 10% compared with the source void fractions when there was no big bubble in the path of light to the detector (or camera).
2. The measured bulk void fractions with the simplified method were in good agreement with those predicted by the slip ratio model and the $k\alpha_H$ model, within the relative error of 22% and 14% for the two models, respectively.

These results are helpful for further optimization of the void fraction measurement system.

Although the bulk void fractions were measured within reasonable errors, the incomplet images left a flaw. Those incomplete images must be caused by the deflection of the sheet laser and the fluorescence at the curved nitrogen-water interface: the reflection and refraction of the sheet laser lead to the lost of fluorescence from the illuminated cross-sections when curved interface is available, i.e., the incomplete objects; while the reflection and refraction of the fluorescence lead to the lost of the image parts, i.e. the incomplete images even for the complete objects. It is still a challenge to identify a complete gas–liquid line from an incomplete cross-sectional image, which is necessary to reconstruct the 3D gas–liquid interface. We need to improve the design of the tube window to reduce the deflection of the fluorescence, and make it possible to collect complete information of the image for the reconstruction of the 3D gas–liquid interface.

Acknowledgment

The project was supported by the State Key Laboratory of Optoelectronic Materials and Technologies of Sun Yat-sen University (Grant No.09010-32031623).

We appreciate Dr Navid Borhani for the encouraging discussion about the fluorescence imaging; and Dr Zhao Wang for the guidance of the ZEMAX usage.

ORCID iDs

Liping Huang https://orcid.org/0000-0003-2504-1055

References

[1] Woods RCGRE 1983 Handbook of multiphase systems *Nucl. Technol.* **60** 334

[2] Kim J, Ahn Y C and Kim M H 2009 Measurement of void fraction and bubble speed of slug flow with three-ring conductance probes *Flow Meas. Instrum.* **20** 103–9
[3] Tian D G, Sun L C, Gao F, Liu J Y and Sun B 2012 A study on application of optical probes for the measurement of local parameters in two-phase flow *J. Exp. Fluid Mech.* **26** 91–5
[4] Bertola V 2003 *Modelling and Experimentation in Two-Phase Flow* (Vienna: Springer) (https://doi.org/10.1007/978-3-7091-2538-0)
[5] Winkler J, Killion J, Garimella S and Fronk B M 2012 Void fractions for condensing refrigerant flow in small channels: Part I literature review *Int. J. Refrig.* **35** 219–45
[6] Hibiki T, Mishima K and Nishihara H 1997 Measurement of radial void fraction distribution of two-phase flow in a metallic round tube using neutrons as microscopic probes *Nucl. Instrum. Methods Phys. Res.* **399** 432–8
[7] Canière H, T'Joen C, Willockx A and Paepe M D 2008 Capacitance signal analysis of horizontal two-phase flow in a small diameter tube *Exp. Therm. Fluid Sci.* **32** 892–904
[8] Raghupathi P A and Kandlikar S G 2016 Contact line region heat transfer mechanisms for an evaporating interface *Int. J. Heat Mass Transfer* **95** 296–306
[9] Wojtan L, Ursenbacher T and Thome J R 2005 Measurement of dynamic void fractions in stratified types of flow *Exp. Therm. Fluid Sci.* **29** 383–92
[10] Wojtan L, Ursenbacher T and Thome J R 2004 Interfacial measurements in stratified types of flow. Part II: measurements for R-22 and R-410A *Int. J. Multiphase Flow* **30** 125–37
[11] Ursenbacher T, Wojtan L and Thome J R 2004 Interfacial measurements in stratified types of flow. Part I: New optical measurement technique and dry angle measurements *Int. J. Multiphase Flow* **30** 107–24
[12] Otsu N 2007 A threshold selection method from gray-level histograms *IEEE Trans. Syst. Man Cybernet.* **9** 62–6
[13] Woods RCGRE 1977 *Digital Image Processing* (Prentice Hall International: Addison-Wesley) (http://tainguyenso.vnu.edu.vn/jspui/handle/123456789/42603)
[14] Smith S L 1970 Void fraction in two-phase flow: a correlation based upon an equal velocity heat model *Proc. Inst. Mech. Eng.* **184** 647–64
[15] Woldesemayat M A and Ghajar A J 2007 Comparison of void fraction correlations for different flow patterns in horizontal and upward inclined pipes *Int. J. Multiphase Flow* **33** 347–70
[16] Butterworth D 1975 A comparison of some void-fraction relationships for co-current gas–liquid flow *Int. J. Multiphase Flow* **1** 845–50
[17] Li S, Cai W, Chen J, Zhang H and Jiang Y 2018 Evaluation analysis of correlations for predicting void fraction of condensation hydrocarbon refrigerant upward flow in a spiral pipe *Appl. Therm. Eng.* **140** 716–32
[18] Winkler J, Killion J and Garimella S 2011 Void fractions for condensing refrigerant flow in small channels. Part II: void fraction measurement and modeling *Int. J. Refrig.* **34** 246–62
[19] Rouhani S Z and Axelsson E 1970 Calculation of void volume fraction in the subcooled and quality boiling regions *Int. J. Heat Mass Transfer* **13** 383–93
[20] Quibén J M and Thome J R 2007 Flow pattern based two-phase frictional pressure drop model for horizontal tubes. Part I: diabatic and adiabatic experimental study *Int. J. Heat Fluid Flow* **28** 1049–59
[21] Xia G, Cai B, Cheng L, Wang Z and Jia Y 2018 Experimental study and modelling of average void fraction of gas–liquid two-phase flow in a helically coiled rectangular channel *Exp. Therm. Fluid Sci.* **94** 9–22